ACS APPLIED MATERIALS & INTERFACES

Research Article

www.acsami.org

Efficient ZnO-Based Visible-Light-Driven Photocatalyst for Antibacterial Applications

Raju Kumar, Srinivasan Anandan,* Kaliyan Hembram, and Tata Narasinga Rao

Centre for Nano Materials, International Advanced Research Centre for Powder Metallurgy and New Materials, Hyderabad 500005, India

Supporting Information

ABSTRACT: Herein, we report the development of a ZnO-based visible-light-driven photocatalyst by interfacial charge transfer process for the inactivation of pathogens under visible-light illumination. Surface modification by a cocatalyst on ZnO, prepared by flame spray pyrolysis process is carried out to induce the visible-light absorption in ZnO. Optical studies showed that surface modification of Cu^{2+} induces the visible-light absorption in ZnO by interfacial charge transfer between ZnO and surface Cu^{2+} ions upon light irradiation. The photocatalytic efficiency of pure and modified ZnO is evaluated for the inactivation of pathogens and the decomposition of methylene blue under visible-light illumination. The antibacterial activity of Cu^{2+}-ZnO is several orders higher than pure ZnO and commercial Degussa-P25 and comparable with Cu^{2+}-TiO_2. Cu^{2+}-ZnO nanorods show better photocatalytic activity than Cu^{2+}-ZnO nanosphere, which is attributed to high surface area to volume ratio of former than later. The holes generated in the valence band and the Cu^{1+} species generated during the interfacial charge transfer process may attribute for the inactivation of bacteria, whereas the strong oxidation power of hole is responsible for the decomposition of methylene blue. Besides the advantage of Cu^{2+}-modified ZnO for visible-light-assisted photocatalytic applications, the method (FSP) used for the synthesis of ZnO in the present study is attractive for commercial application because the process has potential for the production of large quantities (2−3 kg/h) of semiconductors.

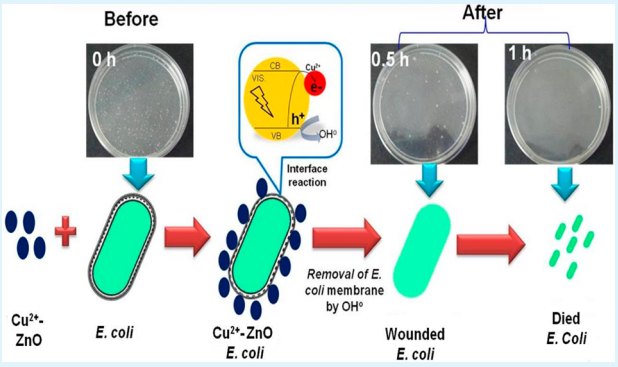

KEYWORDS: *ZnO, photocatalysis, cocatalyst, degradation, antibacterial activity*

1. INTRODUCTION

Currently, the development of visible-light-active materials is in high demand for indoor applications including self-cleaning, air-purification, antipathogen, and water splitting application as these materials can be active either in indoor light or solar light illumination. Particularly, it is essential to develop materials for the removal of infectious pathogens, existing in an indoor air environment, which can cause adverse effects on human health.[1] Though traditional methods such as chlorination,[2] ozone,[3] UV radiation,[4] and advanced filtration processes are available to remove pathogens, they are carcinogenic, expensive and are not eco-friendly. Alternative to these processes, photocatalysis is regarded as a promising approach for environmental remediation including the removal of volatile organic compounds (VOC)[5−16] and pathogens.[17,18] In general, wide-band gap semiconductors such as TiO_2, ZnO, and $SrTiO_3$ are considered as efficient photocatalysts because of their high redox potential of photocharge carriers. Particularly, zinc oxide chosen for this study is attractive because it is a low-cost wide-band gap semiconductor (~3.37 eV), alternative to TiO_2, and its photocatalytic activity was better than TiO_2 in some of the reports.[19−21] Though UV assisted semiconductor photocatalytic oxidation is extensively studied for the removal of pathogens, the development of materials which can function under indoor light sources which do not emit UV light is very important for indoor air purification, particularly for the removal of pathogens. Hence, numerous efforts such as doping of cations[22] and anions[23−26] into wide-band gap semiconductors have been studied to extend the light absorption of semiconductors from UV to visible-light region. Though these attempts are successful partly to induce visible-light absorption in semiconductors, they fail to constitute an efficient visible-light photocatalyst, because the reactivity of photogenerated charge carriers in doped levels or narrowed bands are much less than those in valence band (VB) and conduction band (CB). Very recently, surface modified semiconductors[5−11] have been developed, and they exhibit better visible-light photocatalytic activity due to an efficient interfacial charge transfer (IFCT)[27−31] of VB electrons upon visible-light illumination and multielectron reduction reactions of oxygen[8,32] during which the excited electrons are consumed. For example, doped TiO_2 or ZnO[12−16] that was inactive under

Received: May 15, 2014
Accepted: July 10, 2014
Published: July 16, 2014

   dx.doi.org/10.1021/am502915v | ACS Appl. Mater. Interfaces 2014, 6, 13138−13148

visible-light became an efficient material after Cu^{2+}-modification because of the charge transfer between photogenerated electrons from doped levels to the surface Cu^{2+}-ions. Our novelty in the present study is the development of efficient ZnO based materials through IFCT process for antipathogenic applications under visible-light illumination. Previous studies indicated that UV-assisted semiconductors, the surfaces of semiconductors modified with functional materials including silver and inorganic adsorbents, were being extensively used for antibacterial properties under UV light irradiation.[33] Recently, Miyauchi et al.[34] investigated the antipathogenic activity of hybrid Cu_xO/TiO_2 nanocomposites and concluded that nanometer sized Cu_xO clusters on TiO_2 acts as an excellent risk-reduction material under indoor environment. To the best of our knowledge, the antibacterial properties of surface modified ZnO photocatalysts by IFCT has not been reported so far, though the photocatalytic effects have been investigated for the decomposition of volatile organic compounds (VOCs). In the present study, we have used large scale process synthesized ZnO for surface modification, as the scalable process is very important to extend the use of nanomaterials for commercial applications. Moreover, large quantities of material are prerequisite to overcome market price of nanomaterial and make technology viable for real applications. Previously, ZnO nanoparticles were synthesized by various methods including wet chemical precipitation,[35] sol−gel,[36] solvothermal/hydrothermal,[37] spray pyrolysis,[38] RF plasma,[39] and flame spray pyrolysis.[40] However, each method had its own problems and limitations. Particularly, most of the wet chemical methods have issues like difficulties in controlling the size and morphology, small quantities of yield, longer synthesis time, need for additional catalysts/surfactants, and further these methods required post synthetic heat treatment to acquire crystallinity of the material. In contrast, flame spray pyrolysis (FSP), found to be a suitable process for the synthesis of large-scale nanomaterial as it is an eco-friendly, low-cost, single-step process, and it does not require a post synthetic heat treatment.[40] Most importantly, this method can produce large quantities of nanomaterials that will be attractive for commercial applications. Further, in this method the size and morphology of the nanomaterials can be easily controlled by varying the solvent and synthesis conditions. The interesting characteristics of the material developed in the present study are (i) the antibacterial activity by IFCT process; (ii) the nontoxic, inexpensive, and abundant nature of elements (Cu^{2+} and Zn^{2+}); (iii) formation of nanosphere and nanorod ZnO with excellent textural parameters; (iv) the stability of Cu^{2+}-ZnO under dark as well as light illumination; and (v) the production of a large quantity of ZnO nanoparticles. The photocatalytic activity of pure and modified ZnO is evaluated for the inactivation of pathogens and the decomposition of methylene blue under visible-light illumination. The influence of nanostructures for the removal of pathogens and the stability of material during photocatalysis are discussed in the manuscript.

2. EXPERIMENTAL SECTION

2.1. Preparation of Visible-Light-Active ZnO Photocatalysts. First, the synthesis of ZnO nanostructures (rod and spherical) powders were carried out by custom-made FSP[40] (Friedli AG, Switzerland) instrument. In a typical process, zinc nitrate hexahydrate (98%, Sigma-Aldrich) was used as a precursor that was dissolved in methanol/ethanol (99.95%, Standard Reagent Pvt. Ltd., India) to prepare the solutions in which the Zn^{2+} concentration was 0.94 mol L^{-1}. Methanol was used as a solvent for synthesis of ZnO nanospherical (ZNS) powders where as ethanol was used as a solvent for the synthesis of ZnO nanorod (ZNR). The precursor solution was delivered at the rate of 8 l/h through the 0.8 mm inner diameter capillary of a commercial two phase atomizer (Series 970, Düsen-Schlick, Germany) with the well arrangement of microgear pump (HNP Microsystem, Germany) and the precursor solution dispersed with 80 l/min of oxygen at the 2−3 bar pressure drop. The sprayed precursor was ignited and form the particles with the pilot flame, surrounded the nozzle with feed rate of 5 l/min of methane (inner annulus) and 10 l/min of oxygen (outer annulus). The nanoparticles synthesized by FSP were later used for cocatalyst modification. Co-catalyst (Cu^{2+}) modification on ZnO nanoparticles was done by impregnation method[5] using $CuCl_2.2H_2O$ (Alfa Aesar) as the source for Cu^{2+}. In a detailed synthesis, one gram of ZnO was dispersed in 10 g of distilled water. $CuCl_2{\cdot}2H_2O$ was weighed so that the weight fraction of Cu relative to ZnO was 1×10^{-3} (i.e., 1.57×10^{-5} mol of Cu). The weighed $CuCl_2{\cdot}2H_2O$ was then added to the aqueous suspension containing ZnO heated at 90 °C for 1 h. The resulting suspension was filtered twice with 300 mL water each using a membrane filters (0.025 μm, Millipore) and dried at 60 °C overnight. Finally the samples were grinded using agate mortar and pestle to get fine powder of Cu^{2+}-modified ZnO photocatalyst. The various concentration of Cu^{2+}-ions (0.05, 0.1, and 0.3 wt %) was used for cocatalyst modification to find out the optimum Cu^{2+} for better pathogenic activity. Nanorod and nanosphere ZnO particles were used for cocatalyst modification and named as Cu^{2+}-ZNR and Cu^{2+}-ZNS, respectively.

2.2. Characterization. X-ray Diffraction (XRD) measurement was conducted with Bruker AXS D8 advance system using Cu Kα radiation (λ = 1.5406 Å) over the range of 2θ between 10 and 80 degree at room temperature. The grain size of the photocatalysts was calculated using Scherrer's equation:[41] $D_p = 0.9\lambda/(\beta_{1/2} \cos \theta)$, where D_p is the average grain size in Å, $\beta_{1/2}$ the full width of the peak at half-maximum, and θ is the diffraction angle. The specific surface area, pore volume, and pore diameter of the materials (BET) were performed by surface area and porosity analyzer (Micromeritics ASAP 2020, V3.00 H). The optical properties of the ZnO materials were analyzed by a spectrophotometer (Varian Carry 5000, UV−vis NIR), in which $BaSO_4$ was used for background subtraction. The band gap energy was calculated by the following equation[42] $(\alpha h\nu) = A(h\nu - E_g)^{1/2}$ where α is the absorption coefficient, $h\nu$ is the photon energy, A is constant, and E_g is the band gap energy for direct transitions. The morphology of the samples was measured by field emission scanning electron microscope (FE-SEM, S-4300-SE/N microscope, Hitachi, Japan) and high-resolution transmission electron microscope (HR-TEM, TECNAI-200 kV, FEI Netherlands). Before FE-SEM analysis, the materials were coated with a thin gold layer by sputtering process to make them conducting. X-ray photoelectron spectroscopy (XPS) analysis was acquired to analyze the surface chemistry (oxidation states and the elemental compositions) of the materials using ESCA -Omicron XPS system with Mg−K α as the excitation source.

2.3. Photocatalytic Activity. *Escherichia coli* (*E. coli*, strain No.2251, MTCC, Chandigarh, India) was used as a test pathogen to assess the photocatalytic efficiency of the photocatalysts. A bacterial suspension of *E. coli* was prepared by cultivating the bacteria for overnight. Initially, 50 mL of phosphate buffer solution was added to 50 mg of either pure ZnO or modified ZnO. The resulting suspension was sonicated for 1 h for complete disintegration. Then, the suspension was transferred to the sterilized Petri dish in which 0.5 mL of cultivated *E. coli* was added. The resulting suspension was illuminated for 1 h under blue-LED, which emits the light of wavelengths in the range between 400 and 500 nm with λ_{max} at 456 nm. The light intensity measured by spectro-radiometer (Instrument systems) was ~15 mW/cm^2. The suspension was under magnetic stirring continuously to avoid the sedimentation of suspended particles. At different interval (0, 0.5, and 1 h), the samples were withdrawn from the Petri dish and were diluted. The diluted suspension was placed in a Petri dish to cultivate the bacteria for 24 h at 37 °C, later the bacteria grown on Petri dish was monitored. The

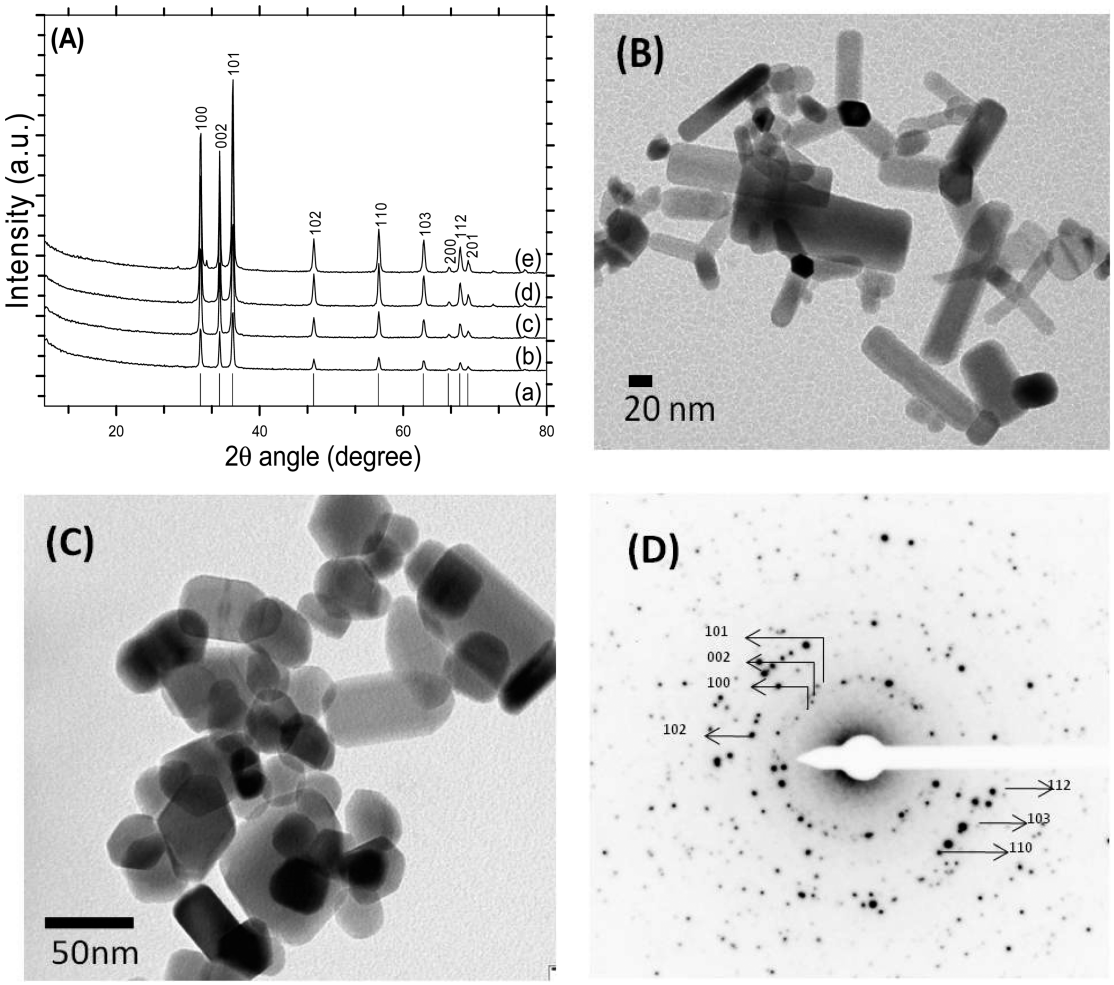

Figure 1. (A) XRD patterns of (a) standard ZnO, (b) pure ZNR, and (c–e) 0.05, 0.1, and 0.3 at % of Cu^{2+}-modified ZNR; HR-TEM images of (B) Cu^{2+}-modified ZNR, and (C) ZNS; and (D) selective area diffraction pattern for Cu^{2+}-modified ZNR.

percentage of surviving bacteria was quantified to determine the efficiency of pure and Cu^{2+}-ZNR/ZNS. The photocatalytic efficiency of ZNR and Cu^{2+}-modified ZNR sample was further investigated by the degradation of MB under the visible-light illumination. Fifty milliliters of aqueous MB solution with the concentration of 0.01 mM was added to 50 mg of either pure or modified ZNR and the suspension was kept in dark for 30 min to reach adsorption–desorption equilibrium before illumination. The natural solar light with/without UV-cutoff filter was used as a visible-light/UV light source, respectively, for photocatalytic experiment. The suspension was illuminated under solar light with continuous magnetic stirring. At a certain time interval during the experiment, the absorbance values of MB solution were measured by a spectrophotometer (model PerkinElmer, Lambda-650 UV/vis). Before each absorbance measurement, the material with MB suspensions were stored in the dark for 2 h to reconvert the reduced methylene blue of the leuco form (LMB) into its initial state.[43−47] With this procedure, changes in absorbance values can be ascribed to the level of MB decomposition from the oxidation reaction. The peak absorbance value of MB appeared at 664 nm, and the change of absorbance was measured at peak value on a spectrophotometer. The concentration of MB was monitored by UV–vis spectrophotometer (model PerkinElmer, Lambda-650 UV/vis) in the wavelength range of 400–800 nm. To check the stability of ZnO or Cu^{2+}-ZnO, XRD analysis was carried out for materials before and after photocatalytic reaction. After photocatalytic reaction, the aqueous suspension of pure or surface modified ZnO was collected by filtration. Then it was washed with water, dried at 80 °C, and the resultant material structure was studied by XRD analysis. To analyze the leaching of Cu^{2+}-ion, 50 mg of Cu^{2+}-ZnO was added into a beaker containing 50 mL of water kept at neutral condition. We carried out the leaching test at neutral pH, because all of the photocatalytic experiments in the present study was carried out at neutral conditions. The resulting mixture was continuously stirred 3 days under dark as well as under visible-light illumination, and the sample was collected from the mixtures after 3 days. The collected samples were centrifuged, and filtered by cellulose acetate syringe filter. Then 5 mL of filtered solution was used for the elemental analysis. The concentration of Cu in the above solution was analyzed by using high sensitive radio frequency inductive coupled plasma (rf-ICP Optical Emission Spectrometer, Varian 720-ES). The quantification limit of rf-ICP instrument for Cu element is about 0.01 ppm. Cu (1000 ppm, ICP Multielement Standard Solution IV, Merck) solution was used as standard and diluted to 0.01, 0.02, 0.04, 0.1, and 0.5 ppm solution for rf-ICP analysis.

3. RESULTS AND DISCUSSION

The XRD patterns and HR-TEM images of ZNR and Cu^{2+}-ZNR are shown in panels A and B in Figure 1, respectively. The diffraction pattern of pure ZNR (b in Figure 1A) is good agreement with the patterns of standard ZnO (ICDD 04–007–1614, a in Figure 1A). The peaks at 2θ = 31.71, 34.40, 36.19, 47.45, 56.51, 62.78, 65.77, 67.86, and 68.96° are assigned to 100, 002, 101, 102, 110, 103, 200, 112, and 201 plane of wurtzite phase of ZnO. The XRD patterns (c–e in Figure 1A) of ZNR with different concentrations of Cu^{2+} (0.05, 0.1, and 0.3 at %) also reveal the presence of wurtzite structure with

Table 1. Physico-chemical Characteristics of ZNR and Cu^{2+}-ZNR

material	lattice parameters		*d*-spacing (Å)	crystal size[a] (nm)	phase	band gap energy[b] (eV)
	a	*c*				
ZNR	3.2529	5.2098	2.478020	93.20	wurtzite	3.2
0.05% Cu^{2+}-ZNR	3.2529	5.2098	2.478020	93.20	wurtzite	3.2
0.1% Cu^{2+}-ZNR	3.2530	5.2130	2.478420	93.45	wurtzite	3.2
0.3% Cu^{2+}-ZNR	3.252 24	5.209 55	2.477600	92.94	wurtzite	3.2

[a] $D_p = 0.9\lambda/\beta_{1/2} \cos\theta$; λ, X-ray source wavelength; $\beta_{1/2}$, full width half-maximum; θ, angle. [b] Band-gap values calculated by plotting photon energy (eV) versus square of absorption co-efficient $(\alpha h\nu)^2$.

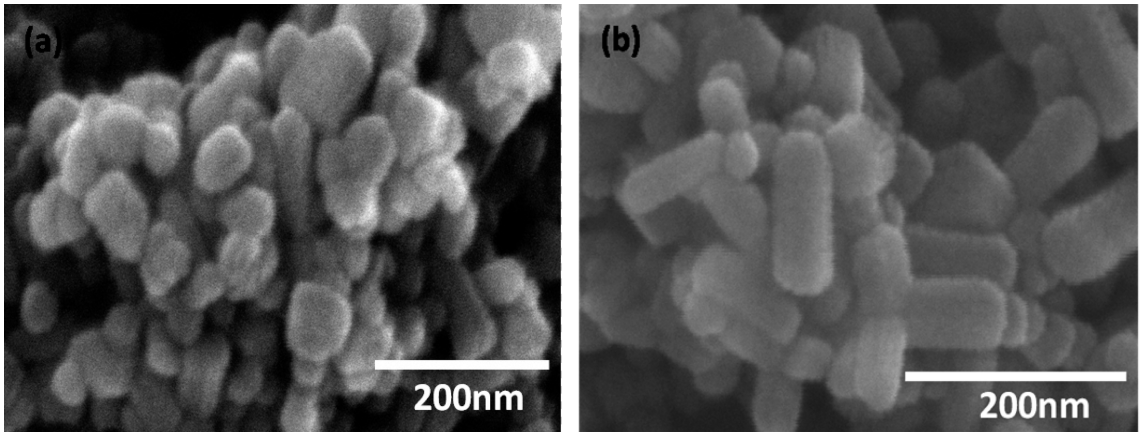

Figure 2. FE-SEM images of (a) Cu^{2+}-modified ZNS and (b) ZNR.

hexagonal phase. These results show that ZNR exhibit single phase hexagonal wurtzite structure without any impurities before and after Cu^{2+}-modification. The XRD patterns of ZNS and Cu^{2+}-ZNS also exhibit the diffraction pattern similar to standard ZnO (see Figure S1 in the Supporting Information). The lattice parameters and *d*-spacing of ZNR/ZNS and Cu^{2+}-ZNR/ZNS are shown in Table 1, and Table S1 in the Supporting Information, and the values are consistent with standard ZnO. The crystal sizes calculated from Debye–Scherrer's equation are 93.2 and 46.3 nm for ZNR and ZNS, respectively. HR-TEM images of Cu^{2+}-ZNR (Figure 1B) shows rodlike structures with diameter and length of ∼15–50 nm and 50–130 nm, respectively. For comparison, we also measured HR-TEM analysis for Cu^{2+}-ZNS and the results are shown in Figure 1C. ZNS image demonstrates the presence of spherical like particles with the diameter of ∼30–100 nm. The HR-TEM images of ZNR and ZNS are shown in the Supporting Information (Figure S2), revealing that the morphologies and sizes of ZNS and ZNR are similar to Cu^{2+}-ZNS and Cu^{2+}-ZNR. A selected area diffraction pattern (Figure 1D) shows (1 0 0), (0 0 2), (1 0 1), (1 0 2), (1 1 0), (1 0 3), (2 0 0), (1 1 2), and (2 0 1) reflections of ZnO, indicating the presence of well-crystallized ZnO in Cu^{2+}-ZNR. FE-SEM images of Cu^{2+}-ZnO are shown in Figure 2. Spherical and distorted spherical-like morphology with particle diameter in the range of 40–80 nm (Figure 2a) is obtained for Cu^{2+}-ZNS, whereas rodlike structure with particle diameter between 40 and 60 nm is obtained for Cu^{2+}-ZNR (Figure 2b). The synthesis mechanism of ZNR and ZNS is explained as follows: When Zn^{2+} precursor solution is introduced into FSP setup, Zn^{2+} solution is atomized into a flame reactor; the liquid precursor then evaporates and undergoes chemical reactions to form cluster-embryos. Then ZnO nanosphere (ZNS) formation takes place by collision-sintering and/or surface growth.[48] On the other hand, the synthesis mechanism of nanorod (ZNR) is different from nanosphere, and it is explained as follows: When ZnO particles encounter maximum flame temperatures of 2400–3000 K, which is higher than the melting point of ZnO (2248 K), ZnO re-evaporates and dissociates into Zn vapor and O_2. As the temperature drops below the ZnO dissociation temperature at the top of the flame because of entrainment of ambient air, the reoxidation of Zn and nucleation in supersaturated flame regions occur. The resulting nuclei now act as seed for surface growth by vapor condensation reaction. Followed by this particle growth by coagulation and sintering takes place to obtain ZNR particles. In the present study, two solvents, namely, ethanol and methanol, have been used for the synthesis of ZnO. The standard heat of combustion of ethanol (used for the synthesis of ZNR) is ∼90% higher than that of methanol (used for the synthesis of ZNS). Hence the low flame temperature and short residence time can be expected in the methanol-based system, which led to the formation of ZNS. In contrast, high flame temperature and long residence time in the ethanol system led to the formation of ZNR. The XPS results are shown in Figure 3. The XPS survey spectrum of Cu^{2+}-ZNR shown in Figure 3a reveals that the material comprises zinc and oxygen. The peak at 284.6 eV corresponds with adventitious elemental hydrocarbon from the XPS instrument itself. We tried to measure the Cu(II) clusters on the surface of ZnO by XPS and HR-TEM analysis. Since the concentration of Cu^{2+}-ion is not in the detectable limit of XPS instrument, we could not detect the Cu (II) clusters. However, EELS analysis clearly reveals the presence of Cu ions in ZnO. Previously Irie et al.[6] investigated the oxidation state of Cu(II) ion in Cu^{2+}-TiO_2 by Cu K-edge X-ray absorption fine structure (XAFS) analysis, and concluded that Cu species exist in the 2+ state and Cu(II) is incorporated in a distorted amorphous CuO structure having a five coordinated square pyramidal form. Because we followed

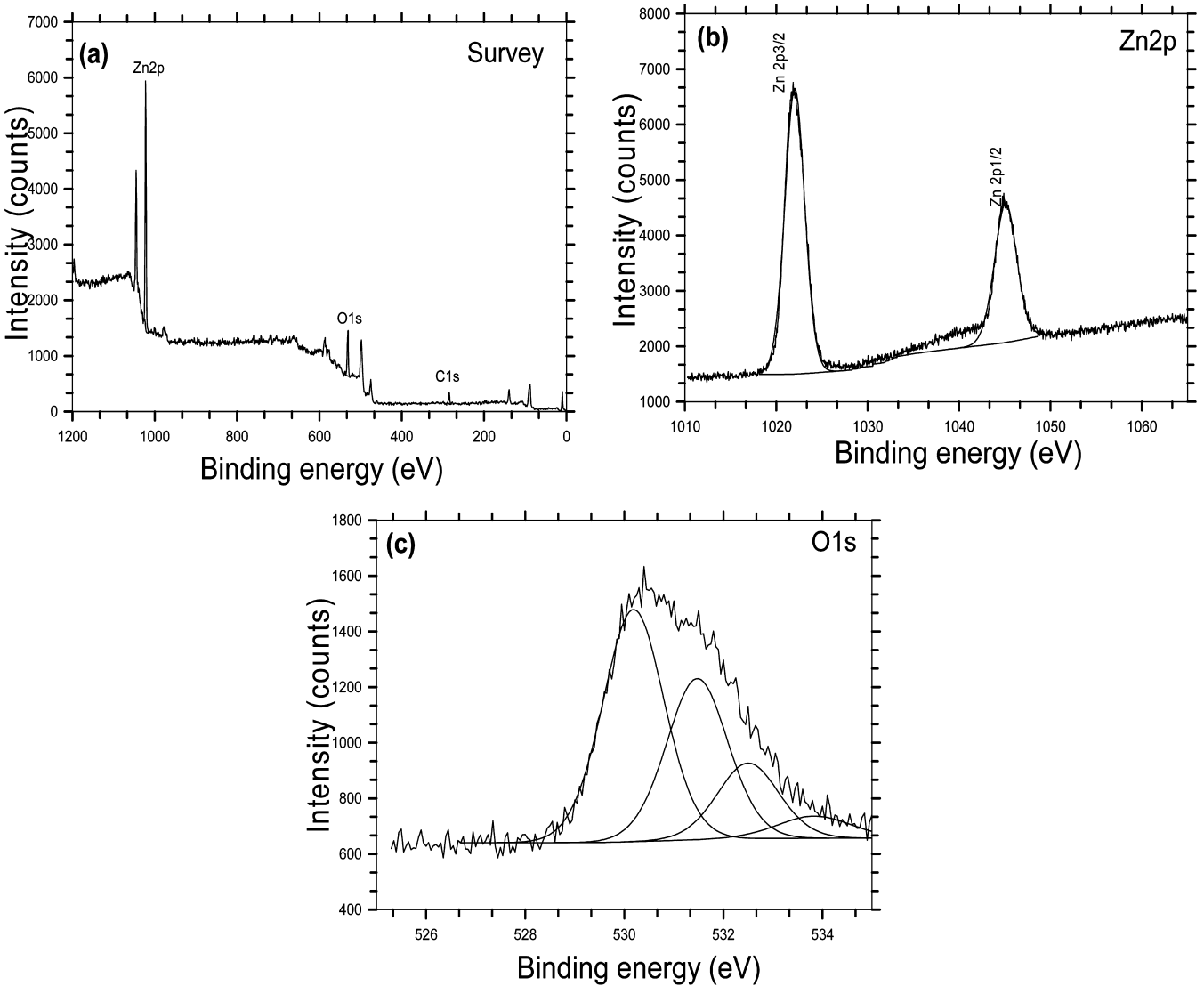

Figure 3. XPS spectrum of Cu^{2+}-modified ZNR; survey spectrum of (a) ZNR, (b) Zn 2p, and (c) O 1s.

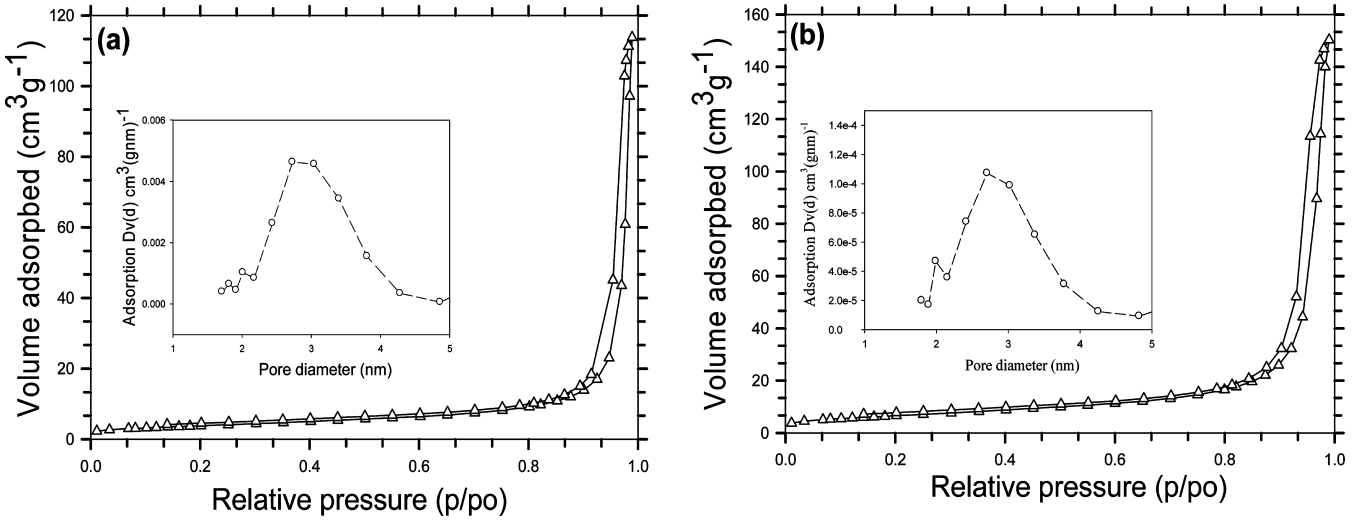

Figure 4. Nitrogen adsorption/desorption isotherm of (a) ZNR and (b) ZNS (inset shows pore size distribution of ZNR and ZNS).

the Cu^{2+}-modification procedure similar to Irie et al., we expect that the Cu^{2+}-ions in this system also should form a distorted CuO like structure with a five-coordinated square pyramidal form. However, the presence of Cu(II) is clearly seen in UV–

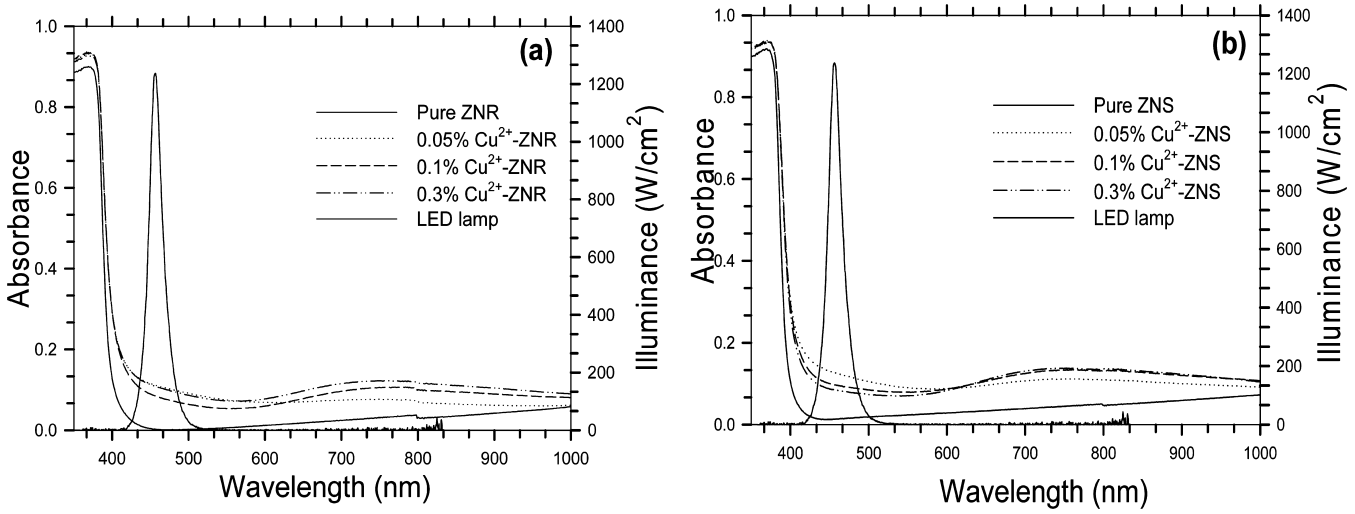

Figure 5. UV−vis spectra of (a) ZNR and Cu^{2+}-modified ZNR and (b) ZNS and Cu^{2+}-modified ZNS.

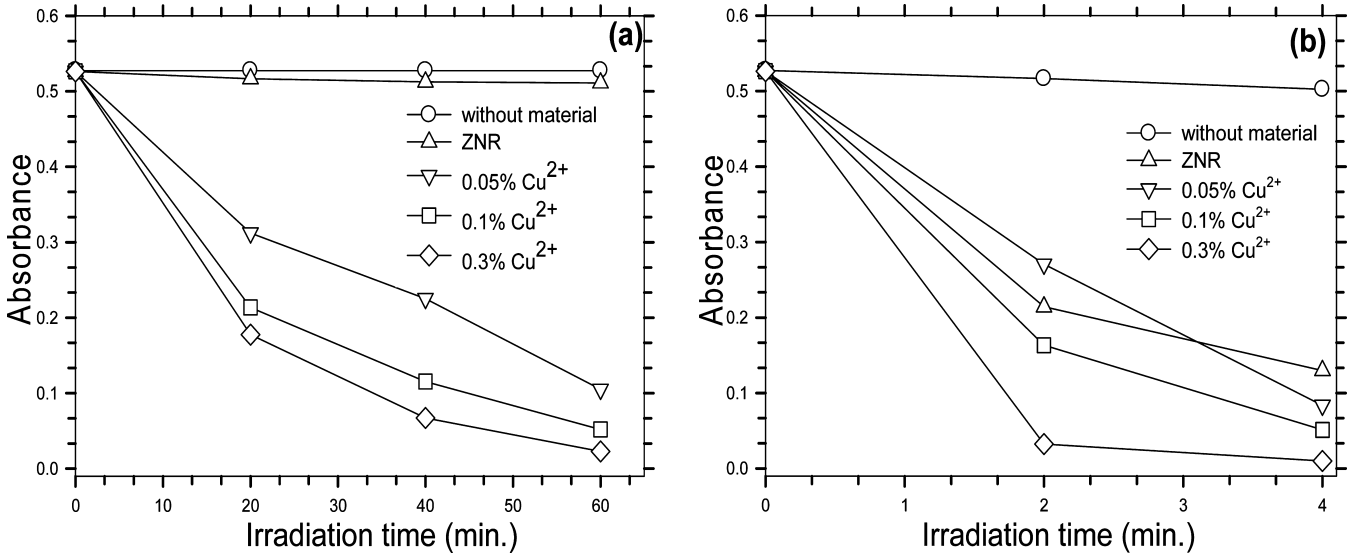

Figure 6. Photocatalytic oxidation of methylene blue (MB) using ZNR and Cu^{2+}-modified ZNR under (a) visible and (b) UV light illumination. Changes in absorbance spectrum of MB as a function of illumination time using Cu^{2+}-modified ZnO is given in the figure.

vis. absorption spectrum of Cu^{2+}-ZnO as shown in Figure 5. Wide scan spectrum of Zn 2p and O 1s shown in Figure 3b and 3c exhibit binding energy peaks of Zn $2p_{3/2}$ at 1021.65 eV; Zn $2p_{1/2}$ at 1044.8 eV, and of O 1s at 530.15 eV respectively. The broad peak of O 1s is due to the surface-adsorbed OH^- ions on the surface of ZnO. The binding energy peak values of Zn 2p and O 1s of Cu^{2+}-ZNR are in good agreement with the values reported previously.[49,50] Wide scan spectral analysis was also carried out for pure ZNR and the results are displayed in the Supporting Information (a−c in Figure S3). The binding energy peaks of Zn 2p3/2 at 1021.25 eV, Zn 2p1/2 at 1044.7 eV, and O 1s at 530.05 eV are consistent with the results of Cu^{2+}-ZNR, revealing that the binding energy characteristics of all materials are similar to standard ZnO. The nitrogen adsorption−desorption isotherms of ZNR and ZNS, shown in Figure 4. ZNR and ZNS exhibit adsorption isotherms similar to Type II,[51] which is often observed when multilayer adsorption occurs on non porous solid. The surface area of ZNR is ∼20.3 m^2 g^{-1}, whereas ZNS exhibit a surface area of 17.3 m^2g^{-1}. The small difference in the surface area between ZNS and ZNR is due to the presence of well-crystalline large particles in the former compared to the latter. The pore size distribution of ZNR and ZNS are shown in insets of panels a and b in Figure 4, respectively. The average pore diameter and pore volume ZNR and ZNS are 2.73 nm, 0.043269 cm^3 g^{-1}, and 2.7 nm, 0.035341 cm^3 g^{-1}respectively. The large pore of ZnO allows an easy diffusion of pathogens in and around the semiconductor, thus it will enhance the adsorption of pathogens and it is intermediate on the surface of the photocatalysts.

The UV−vis diffuse reflectance spectra of pure ZnO (ZNR, ZNS) and Cu^{2+}-ZnO (ZNR, ZNS) are shown in panels a and b in Figure 5. ZNR and ZNS show an absorption onset at ∼380 nm that reveals the typical band-to-band transition characteristics of pure ZnO. When different concentrations of Cu^{2+}-ions are modified onto the surface of ZNR and ZNS, two additional absorption bands appear beside interband transition. The small absorption ranging from 400 to 500 nm corresponds with interfacial charge transfer (IFCT)[5−11,27−32] from the excitation of electrons from the valence band (VB) of ZnO to Cu^{2+} ions.

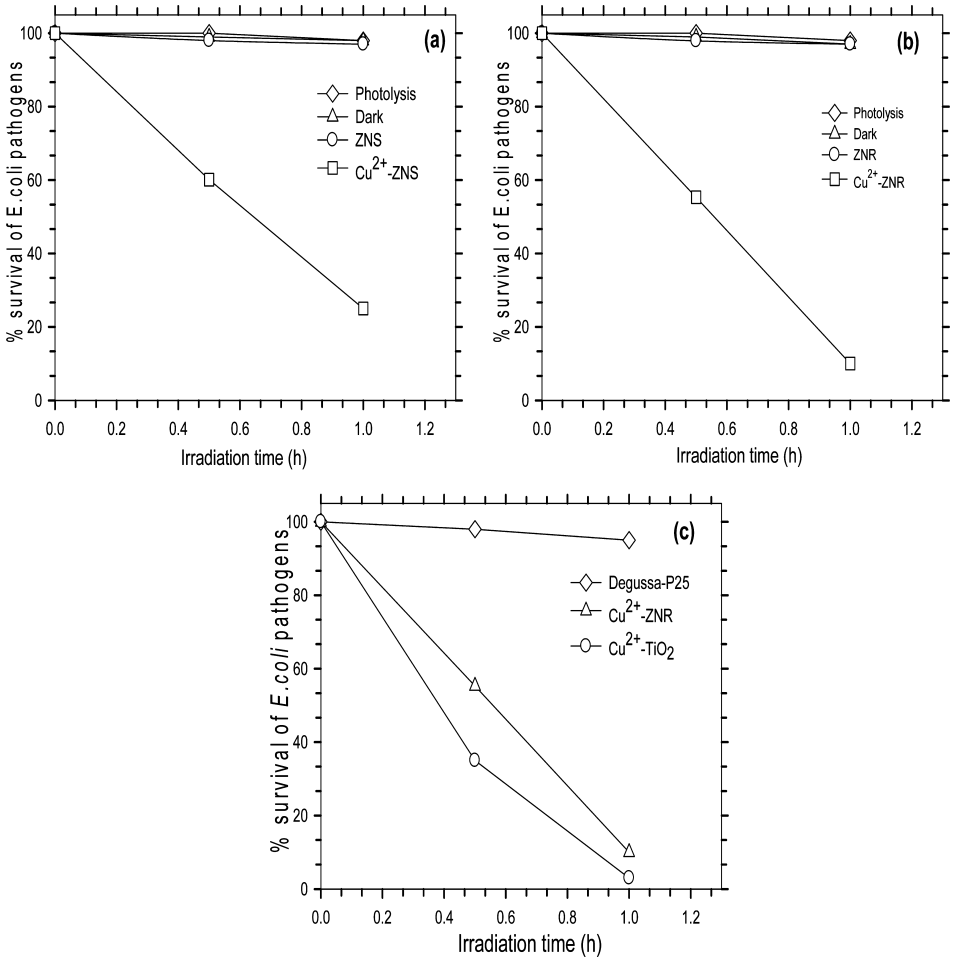

Figure 7. Percentage survival of *E. coli* pathogens vs illumination time for the inactivation of pathogens using (a) ZNS & Cu^{2+}-modified ZNS, (b) ZNR & Cu^{2+}-modified ZNR, and (c) Cu^{2+}-modified ZNR, Degussa P-25 & Cu^{2+}-TiO_2. For comparison the results of photolysis, and dark also included in the figure.

The strong absorption at ∼700−800 nm belongs with d−d transition[52] of Cu^{2+} ions. The band gap energies of ZnO before and after Cu^{2+}-modification were calculated and the band gap diagrams and values are shown in Figure S4 and Table S1 in the Supporting Information and Table 1. All ZnO (ZNR, ZNS) and Cu^{2+}-ZnO (ZNR, ZNS) exhibit the band gap energy of ∼3.2 eV, which is in good agreement with the band gap energy value of standard ZnO. This also reveals that there is no change in the band gap of ZnO as Cu^{2+} addition into ZnO is purely a surface modification. It is interesting to note that the absorption spectrum of Cu^{2+}-ZnO in the wavelength region ∼400−500 nm matches well with the spectrum of LED lamp, whereas the absorption spectrum of d-d transition does not cover the wavelength range of LED lamp. Hence it is expected that only the absorption at ∼400−500 nm (IFCT) may contribute for the visible-light activity of Cu^{2+}-ZnO rather than ∼ the absorption at 700−800 nm (d−d transition).

Initially, we evaluated the photocatalytic decomposition of our materials for the degradation of organic pollutants under visible-light illumination. Figure 6 shows the results for the degradation of MB using ZNR/ZNS and Cu^{2+}-modified ZNR/ZNS with different content of Cu^{2+}-ions under visible-light illumination. The direct decomposition of methylene blue without materials was not detected under light illumination in a control experiment. Pure ZnO photocatalysts showed negligible visible-light photocatalytic activity (Figure 6a), which is due to the large band gap of ZnO and the lack of absorption in the visible region. In contrast, the Cu^{2+}-modified ZNR samples exhibited higher photocatalytic activities than pure ZNR photocatalyst as shown Figure 6a. The Cu^{2+}-modified ZNR exhibited visible-light photocatalytic activity because of IFCT.[5] Cu^{2+}(0.05 to 0.3%)-modified ZNS also show high photocatalytic activity (Figure 6b) in comparison with pure ZNS, which is consistent with the trend observed for pure ZNR or Cu^{2+}-modified ZNR. For comparsion, we also evaluated the efficiency under UV-light illumination and the results demonstrated that Cu^{2+}-modified ZNR/ZNS exhibit excellent photocatalytic activity than pure ZNR/ZNS. The results (Figure S5) and the respective discussion can be seen in the Supporting Information.

E. coli was chosen as test pathogen to assess the efficiency of ZnO and modified ZnO under visible-light (blue LED) illumination. The aqueous suspension containing *E. coli*, ZnO, and phosphate buffer solution is placed in a Petri dish and the resulting suspension was irradiated by blue LED lamp. The number of surviving bacteria in terms of colony forming units (CFU) was quantified at different time intervals for each material. The percentage survival of *E. coli* pathogens after photocatalytic experiment as a function of illumination time has been calculated and the results are shown in Figure 7. To know the effect of photolysis (blue LED alone) over bacterial growth of *E. coli*, the experiment was also done only by light

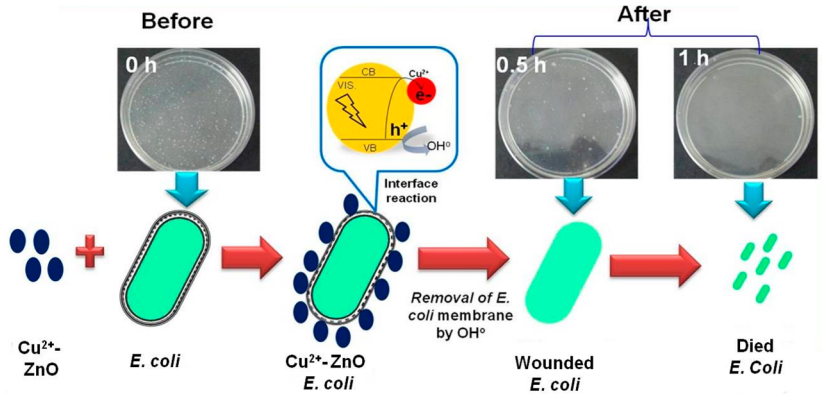

Figure 8. Schematic illustration for the mechanism of degradation of pathogens by Cu^{2+}-modified ZnO under blue LED illumination.

illumination without adding material into the *E. coli* containing suspension and the results are also included in Figure 7. The results of photolysis (without material) show the same number of *E. coli* pathogens before and after LED illumination, revealing that LED illumination alone does not affect the bacterial growth even after 5 h. ZNR and ZNS show negligible bactericidal activity as ZnO is large band gap semiconductor. In contrast to ZnO and photolysis, the survival of *E. coli* pathogens decrease rapidly even at 0.5 h of illumination for Cu^{2+}-ZNR and Cu^{2+}-ZNS. The percentage survival of *E. coli* pathogens of Cu^{2+}-ZNR and Cu^{2+}-ZNS shows several orders higher than pure ZnO after 1 h illumination. At the end of 1 h illumination the pathogens are completely inactivated and hence negligible growth of pathogens is observed. For comparison, we have also carried out the antibacterial experiment using Cu^{2+}-ZnO (ZNS/ZNR) under dark condition as a control experiment and the results are shown in Figure 7. As can be seen in panels a and b in Figure 7, Cu^{2+}-ZnO showed a negligible bacterial inactivation in the dark, whereas significant inactivation of *E. coli* obtained under visible-light illumination as a result of an interfacial charge transfer (IFCT) process. It was reported[34] that Cu-ion in 2+, and 0 oxidation state showed negligible bactericidal activity in dark in comparison with Cu-ion in Cu^{1+} oxidation state. It is also reported[53] that Cu^{2+}-ion is active in the dark only in the presence of hydrogen peroxide. On the basis of these results, it is concluded that Cu^{2+}-ZnO is active only for the inactivation of *E. coli* under visible-light illumination. Moreover, it is interesting to note that the photocatalytic activity of Cu^{2+}-ZNR is slightly higher than Cu^{2+}-ZNS, showing that high surface to volume ratio of ZNR than ZNS is the reason for high photocatalytic activity. The surface areas and average pore diameters of ZNR and ZNS are 20.3 and 17.3 $m^2\ g^{-1}$ and 2.73 and 2.7 nm, respectively. The small nanorod particles and large pore of ZnO allows an easy diffusion of pathogens in and around the semiconductor, thus enhancing the adsorption of pathogens on the surface of ZnO, which later effectively decomposed by hole or hydroxyl radical, generated during photocatalytic reaction. For comparison, the bacterial inactivation of *E. coli* was carried out using Degussa-P25, and Cu^{2+}-TiO_2 under similar experimental conditions. The antibacterial activity of Cu^{2+}-ZnO is several orders higher than pure ZnO and commercial Degussa-P25 and comparable with Cu^{2+}-TiO_2. The photocatalytic activities of the materials are in the following order: Cu^{2+}-TiO_2 > Cu^{2+}-ZNR > Cu^{2+}-ZNS > ZNR/ZNS/Degussa P-25. The reason for the enhancement in the photocatalytic activity of Cu^{2+}-modified ZnO over ZnO is schematically illustrated in Figure 8. ZnO consists of O 2p orbital of valence band (VB) and Zn 4s orbital of conduction band (CB). The distance between the VB (O 2p) and the CB (Zn 4s) of pure ZnO is ~3.2 eV, and hence it can absorb major part of UV light. Pure ZNR and ZNS are inactive due to lack of absorption in visible-light region. When ZNR/ZNS modify with Cu^{2+}-ions, it induces visible-light absorption in ZnO by IFCT and also acts as a cocatalyst to reduce the oxygen molecules efficiently. In general, it has been expected that the mechanism of the antibacterial activity of metal oxide is due to interaction with highly reactive oxygen species (ROS), which causes oxidative damage of the cell membrane or inside the cells.[54,55] These ROS contains hydroxyl groups, superoxide anions ($O_2^{\bullet -}$) and hydrogen peroxide H_2O_2.[56] It was reported that antioxidant enzymes can protect the mitochondria against damage from ROS. However, when excess ROS is produced during reaction, the natural antioxidant defenses may be overwhelmed,[57] which causes several subcellular injuries such as protein denaturation, membrane, and DNA damage. In the present study, when visible-light illuminates on Cu^{2+}-ZnO, the electron in the valence band of ZnO are excited to Cu^{2+}-ions in nanoclusters through an IFCT process. The excited electrons reduce Cu^{2+} into Cu^{1+} and thereby reduce the oxygen molecules through multielectron reduction, whereas holes in the valence band decompose organic pollutants because of their high oxidation power.[14,15] It was reported[34] that upon visible-light illumination in Cu_xO/TiO_2 system, holes generated in the valence band of TiO_2 in combination with Cu^{1+} -ions can damage outer membrane of viruses and bacteria. On the basis of these results it is presumed that strong oxidation power of holes generated in the valence band responsible for the decomposition of methylene blue, whereas holes in combination with Cu^{1+}ions responsible for the inactivation of pathogens under visible-light illumination. One of the most important findings of the present study is that this is the first discovery of the development of efficient ZnO-based materials through IFCT for antipathogenic applications under visible-light illumination.

Considering the importance of the stability of a photocatalyst in practical applications, the photocatalytic stability of the ZNR and ZNS before and after photocatalytic reaction was investigated by structural (XRD) analysis. The results reveal that XRD patterns of ZnO (ZNR and ZNS) and Cu^{2+}-modified ZnO (ZNR and ZNS) (Figure 9 and Figure S6 in the Supporting Information) after photocatalytic reaction is similar to the one before photocatalytic reaction. The XRD patterns of ZNR and Cu^{2+}-modified ZNR before and after photocatalytic reaction are consistent with the pattern of standard ZnO

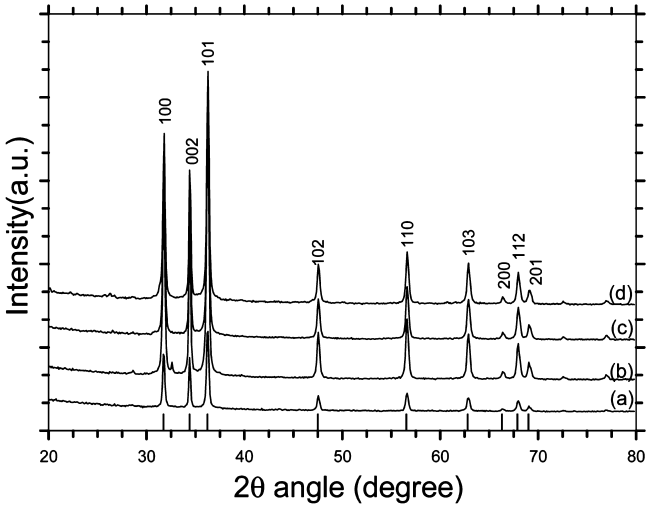

Figure 9. XRD patterns of ZNR and Cu^{2+}-modified ZNR (a, b) before and (c, d) after antibacterial experiment, respectively.

(ICDD 04−007−1614). These results reveal that there was no change in the structure of ZnO and Cu^{2+}-modified ZnO, indicating that ZnO behaves as stable visible-light semiconductor. Recently, Anandan et al.[14−16] reported that Zn^{2+} ions in ZnO photocatalysts were not dissolved in water at neutral conditions during exposure of visible-light (blue LED) and dark for short- as well as long-term. Because we followed identical experimental conditions, we presume that ZnO used in the present study is also stable under visible-light illumination. Moreover, Irie et al.[6] investigated the role of Cu^{2+} cocatalyst by X-ray absorption fine structure (XAFS) analysis. In situ XAFS measurements were performed under visible-light in the presence of 2-propanol and absence of oxygen. Under these conditions, Cu^{1+} was generated. However, it later converted back to Cu^{2+} when it was exposed to oxygen, indicating the oxygen reduction activity of Cu^{1+}. These results clearly show that the electrons in Cu^{1+} ions can cause the reduction reaction of absorbed oxygen molecules. Very importantly, the Cu^{2+}-ions were not changed in air condition, even after the photocatalytic oxidative reaction, and the turnover numbers of this reaction is more than 4. It means that the Cu^{2+}-ion is a very stable cocatalyst during photocatalytic reaction. rf-ICP analysis revealed that Cu^{2+} ions on ZnO photocatalyst was not dissolved in water during the exposure of visible-light as well in dark even after 3 days, because the Cu(II) is incorporated on ZnO as distorted amorphous CuO-like structure, having a five coordinated square pyramidal form. Since these distorted CuO clusters are strongly attached to the ZnO surface, the Cu^{2+}-ions are not leaching from ZnO during photocatalytic reaction. The present result indicates that Cu^{2+}-ZnO act as a stable visible-light-driven photocatalyst under visible-light illumination at neutral condition.

4. CONCLUSION

In summary, we have prepared an efficient ZnO-based visible-light-driven photocatalyst by adopting interfacial charge transfer process for the inactivation of *E. coli* under visible-light illumination. ZnO nanoparticles, synthesized by a large-scale flame spray pyrolysis process was used for surface (Cu^{2+}) modification. Optical studies show that Cu^{2+} ions induce visible-light absorption in ZnO, while pure ZnO exhibits typical band to band transition. Characterization studies reveal the presence of spherical and rod like wurtzite phase ZNS and ZNR respectively. ZNR/ZNS shows less photocatalytic activity, whereas Cu^{2+} addition onto ZNR/ZNS drastically increases their efficiency. The antibacterial activity of Cu^{2+}-ZnO is several orders higher than pure ZnO and commercial Degussa-P25 and comparable with Cu^{2+}-TiO_2. The Cu^{2+}-ZnO nanorod shows better photocatalytic activity than the Cu^{2+}-ZnO nanosphere, which is attributed to the high surface area to volume ratio of the former than later. The holes generated in the valence band and the Cu^{1+} species generated during the IFCT process may attribute for the inactivation of bacteria, whereas the strong oxidation power of hole is responsible for the decomposition of methylene blue. The stability analysis confirms that the Cu^{2+}-ZnO is stable in aqueous solution under dark as well as visible-light illumination at neutral conditions. In summary, the developed visible-light photocatalyst may be promising for pathogenic application in indoor environment like hospitals, airports, schools, and railway stations.

■ ASSOCIATED CONTENT

Ⓢ Supporting Information

Table S1, physico-chemical characteristics of ZNS and Cu^{2+}-ZNS; Figure S1, XRD patterns of (a) standard ZnO (ICDD 04−007−1614), (b) pure ZNS, and (c−e) 0.05, 0.1, and 0.3% of Cu^{2+}-modified ZNS; Figure S2, HR-TEM images of ZnO (a) ZNS and (b) ZNR; Figure S3, XPS spectrum of pure ZNR (a) survey spectrum of ZNR, (b) Zn 2p, and (c) O 1s; Figure S4, The band gap calculation for (a) ZNS and Cu^{2+}-ZNS, (b) ZNR and Cu^{2+}-ZNR; Figure S5, photocatalytic oxidation of methylene blue (MB) using ZNS and Cu^{2+}-modified ZNS under (a) visible and (b) UV light illumination; Figure S6, XRD patterns of ZNS and Cu^{2+}-modified ZNS (a and b) before and (c and d) after antibacterial experiment, respectively. This material is available free of charge via the Internet at http://pubs.acs.org/.

■ AUTHOR INFORMATION

Corresponding Author

*E-mail: anandan@arci.res.in.

Notes

The authors declare no competing financial interest.

■ ACKNOWLEDGMENTS

The authors are thankful to Dr. G. Sundararajan, Director, ARCI, for his keen interest and encouragement in carrying out this work. The authors are thankful to Dr. S. Sakthivel and Mr. M. Ramakrishna, ARCI, for their help to measure UV-DRS and HR-TEM, respectively.

■ REFERENCES

(1) Morens, D. M.; Folkers, G. K.; Fauci, A. S. The Challenge of Emerging and Re-emerging Infectious Diseases. *Nature* **2004**, *430*, 242−249.

(2) Dunlop, P. S. M.; Byrne, J. A.; Manga, N.; Eggins, B. R. The Photocatalytic Removal of Bacterial Pollutants from Drinking Water. *J. Photochem. Photobiol., A* **2002**, *148*, 355−363.

(3) Huang, W. J.; Fang, G. C.; Wang, C. C. The Determination and Fate of Disinfection by-products from Ozonation of Polluted Raw Water. *Sci. Total Environ.* **2005**, *345*, 261−272.

(4) Robertson, J. M. C.; Robertson, P. K. J.; Lawton, L. A. A Comparison of the Effectiveness of TiO_2 Photocatalysis and UVA

Photolysis for the Destruction of Three Pathogenic Micro-organisms. *J. Photochem. Photobiol., A* **2005**, *175*, 51−56.
(5) Irie, H.; Miura, S.; Kamiya, K.; Hashimoto, K. Efficient Visible Light-Sensitive Photocatalysts: Grafting Cu(II) Ions onto TiO_2 and WO_3 Photocatalysts. *Chem. Phys. Lett.* **2008**, *457*, 202−205.
(6) Irie, H.; Kamiya, K.; Shibanuma, T.; Miura, S.; Tryk, D. A.; Yokoyama, T.; Hashimoto, K. Visible Light-Sensitive Cu(II)-Grafted TiO_2 Photocatalysts: Activities and X-Ray Absorption Fine Structure Analyses. *J. Phys. Chem. C* **2009**, *113*, 10761−10766.
(7) Yu, H.; Irie, H.; Shimodaira, Y.; Hosogi, Y.; Kuroda, Y.; Miyauchi, M.; Hashimoto, K. An Efficient Visible-Light-Sensitive Fe(III)-Grafted TiO_2 Photocatalyst. *J. Phys. Chem. C* **2010**, *114*, 16481−16487.
(8) Abe, R.; Takami, H.; Murakami, N.; Ohtani, B. Pristine Simple Oxides as Visible Light Driven Photocatalysts: Highly Efficient Decomposition of Organic Compounds over Platinum-loaded Tungsten Oxide. *J. Am. Chem. Soc.* **2008**, *130*, 7780−7781.
(9) Anandan, S.; Miyauchi, M. Improved Photocatalytic Efficiency for WO_3 System by an Efficient Visible-Light-Induced Hole Transfer. *Chem. Commun.* **2012**, *48*, 4323−4325.
(10) Arai, T.; Horiguchi, M.; Yanagida, M.; Gunji, T.; Sugihara, H.; Sayama, K. Complete Oxidation of Acetaldehyde and Toluene over a Pd/WO_3 Photocatalyst under Fluorescent- or Visible-Light Irradiation. *Chem. Commun.* **2008**, *43*, 5565−5567.
(11) Kim, Y.; Irie, H.; Hashimoto, K. A Visible Light-Sensitive Tungsten Carbide/Tungsten Trioxide Composite Photocatalyst. *Appl. Phys. Lett.* **2008**, *92*, 182107.
(12) Yu, H. G.; Irie, H.; Hashimoto, K. Conduction Band Energy Level Control of Titanium Dioxide: Toward an Efficient Visible-Light-Sensitive Photocatalyst. *J. Am. Chem. Soc.* **2010**, *132*, 6898−6899.
(13) Qiu, X.; Miyauchi, M.; Yu, H.; Irie, H.; Hashimoto, K. Visible-Light-Driven Cu(II)-$(Sr_{1-y}Na_y)(Ti_{1-x}Mo_x)O_3$ Photocatalysts Based on Conduction Band Control and Surface Ion Modification. *J. Am. Chem. Soc.* **2010**, *132*, 15259−15267.
(14) Anandan, S.; Ohashi, N.; Miyauchi, M. ZnO-Based Visible-Light Photocatalyst: Band-Gap Engineering and Multi-Electron Reduction by Co-Catalyst. *Appl. Catal., B* **2010**, *100*, 502−509.
(15) Anandan, S.; Miyauchi, M. Ce-Doped ZnO ($Ce_xZn_{1-x}O$) Becomes an Efficient Visible-Light-Sensitive Photocatalyst by Co-Catalyst (Cu^{2+}) Grafting. *Phys. Chem. Chem. Phys.* **2011**, *13*, 14937−14945.
(16) Anandan, S.; Miyauchi, M. Photocatalytic Activity of Cu^{2+}-Grafted Metal Doped ZnO Photocatalysts under Visible-Light Irradiation. *Electrochemistry* **2011**, *79*, 842−844.
(17) Krasner, S. W.; Weinberg, H. S.; Richardson, S. D.; Pastor, S. J.; Chinn, R.; Sclimenti, M. J.; Onstad, G. D.; Thruston, A. D., Jr. Occurrence of a New Generation of Disinfection Byproducts. *Environ. Sci. Technol.* **2006**, *40*, 7175−7185.
(18) Leung, Y. H.; Chan, C. M.; Ng, A. M.; Chan, H. T.; Chiang, M. W.; Djurisic, A. B.; Ng, Y. H.; Jim, W. Y.; Guo, M. Y.; Leung, F. C.; Chan, W. K.; Au, D. T. Antibacterial Activity of ZnO Nanoparticles with a Modified Surface under Ambient Illumination. *Nanotechnology* **2012**, *23*, 475703.
(19) Wang, G.; Chen, D.; Zhang, H.; Zhang, Z.; Li, J. Tunable Photocurrent Spectrum and Enhanced Photocatalytic Activity of Well-Oriented Zinc Oxide Nanorod Arrays. *J. Phys. Chem. C* **2008**, *112*, 8850−8855.
(20) Arsana, P.; Bubpa, C.; Sang-aroon, W. Photocatalytic Activity under Solar Irradiation of Silver and Copper Doped Zincoxide: Photodeposition versus Liquid Impregnation Methods. *J. Appl. Sci.* **2012**, *12*, 1809−1816.
(21) Sakthivel, S.; Neppolian, B.; Shankar, M. V.; Arabindoo, B.; Palanichamy, M.; Murugesan, V. Solar Photocatalytic Degradation of Azo Dye: Comparison of Photocatalytic Efficiency of ZnO and TiO_2. *Sol. Energy Mater. Sol. Cells* **2003**, *77*, 65−82.
(22) Highfield, J. G.; Pichat, P. Photoacoustic Study of the Influence of Platinum Loading and Bulk Doping with Chromium III Ions on the Reversible Photochromic Effect in Titanium Dioxide. Correlation with Photocatalytic Properties. *New. J. Chem.* **1989**, *13*, 61−66.
(23) Asahi, R.; Morikawa, T.; Ohwaki, T.; Aoki, K.; Taga, Y. Visible-Light Photocatalysis in Nitrogen-Doped Titanium Oxides. *Science* **2001**, *293*, 269−271.
(24) Irie, H.; Watanabe, Y.; Hashimoto, K. Nitrogen-Concentration Dependence on Photocatalytic Activity of $TiO_{2-x}N_x$ Powders. *J. Phys. Chem. B* **2003**, *107*, 5483−5486.
(25) Miyauchi, M.; Ikezawa, A.; Tobimatsu, H.; Irie, H.; Hashimoto, K. Zeta Potential and Photocatalytic Activity of Nitrogen Doped TiO_2 Thin Films. *Phys. Chem. Chem. Phys.* **2004**, *6*, 865−870.
(26) Nakamura, R.; Tanaka, T.; Nakato, Y. Mechanism for Visible Light Responses in Anodic Photocurrents at N-Doped TiO_2 Film Electrodes. *J. Phys. Chem. B* **2004**, *108*, 10617−10620.
(27) Creutz, C.; Brunschwig, B. S.; Suntin, N. Interfacial Charge Transfer Absorption: 3. Application to Semiconductor-Molecule Assemblies. *J. Phys. Chem. B* **2006**, *110*, 25181−25190.
(28) Creutz, C.; Brunschwig, B. S.; Suntin, N. Interfacial Charge Transfer Absorption: Semiclassical Treatment. *J. Phys. Chem. B* **2005**, *109*, 10251−10260.
(29) Hush, N. S. Homogeneous and Heterogeneous Optical and Thermal Electron Transfer. *Electrochim. Acta* **1968**, *13*, 1005−1023.
(30) Hush, N. S. Electron Transfer in Retrospect and Prospect 1: Adiabatic Electrode Processes. *J. Electroanal. Chem.* **1999**, *460*, 5−29.
(31) Hush, N. S. Electron Transfer in Retrospect and Prospect 1: Adiabatic Electrode Processes. *J. Electroanal. Chem.* **1999**, *470*, 170−195.
(32) Zhao, Z. G.; Miyauchi, M. Nanoporous-Walled Tungsten Oxide Nanotubes as Highly Active Visible-Light-Driven Photocatalysts. *Angew. Chem., Int. Ed.* **2008**, *47*, 7051−7055.
(33) Elahifard, M. R.; Rahimnejad, S.; Haghighi, S.; Gholami, M. R. Apatite-Coated $Ag/AgBr/TiO_2$ Visible-Light Photocatalyst for Destruction of Bacteria. *J. Am. Chem. Soc.* **2007**, *129*, 9552−9553.
(34) Qiu, X.; Miyauchi, M.; Sunada, K.; Minoshima, M.; Liu, M.; Lu, Y.; Li, D.; Shimodaira, Y.; Hosogi, Y.; Kuroda, Y.; Hashimoto, K. Hybrid Cu_xO/TiO_2 Nanocomposites as Risk-Reduction Materials in Indoor Environments. *ACS Nano* **2012**, *6*, 1609−1618.
(35) Lingna, W.; Mamoun, M. Synthesis of Zinc Oxide Nanoparticles with Controlled Morphology. *J. Mater. Chem.* **1999**, *9*, 2871−2878.
(36) Bahnemann, D. W.; Kormann, C.; Hoffmann, M. R. Preparation and Characterization of Quantum Size Zinc Oxide: A Detailed Spectroscopic Study. *J. Phys. Chem.* **1987**, *91*, 3789−3798.
(37) Hui, Z.; Deren, Y.; Xiangyang, M.; Yujie, J.; Jin, X.; Duanlin, Q. Synthesis of Flower-Like ZnO Nanostructures by an Organic-Free Hydrothermal Process. *Nanotechnology* **2004**, *15*, 622−626.
(38) Ghaffarian, H. R.; Saiedi, M.; Sayyadnejad, M. A. Synthesis of ZnO Nanoparticles by Spray Pyrolysis Method. *Iran. J. Chem. Chem. Eng.* **2011**, *30*, 1−6.
(39) Peng, H.; Fangli, Y.; Liuyang, B.; Jinlin, L.; Yunfa, C. Plasma Synthesis of Large Quantities of Zinc Oxide Nanorods. *J. Phys. Chem. C* **2007**, *111*, 194−200.
(40) Hembram, K.; Sivaprakasam, D.; Rao, T. N.; Wegner, K. Large-Scale Manufacture of ZnO Nanorods by Flame Spray Pyrolysis. *J. Nanopart. Res.* **2013**, *15*, 1−11.
(41) Hong, R. Y.; Li, J. H.; Chen, L. L.; Liu, D. Q.; Li, H. Z.; Zheng, Y.; Ding, J. Synthesis, Surface Modification and Photocatalytic Property of ZnO Nanoparticles. *Powder Technol.* **2009**, *189*, 426−432.
(42) Vanleeuwen, R. A.; Hung, C. J.; Kammler, D. R.; Switzer, J. A. Optical and Electronic Transport-Properties of Electrodeposited Thallium(III) Oxide-Films. *J. Phys. Chem.* **1995**, *99*, 15247−15252.
(43) Anandan, S.; Rao, T. N.; Sathish, M.; Rengappa, D.; Honma, I.; Miyauchi, M. Supper-Hydrophilic Graphene Loaded TiO_2 Thin-Film for Self-Cleaning Applications. *ACS Appl. Mater. Interfaces* **2013**, *3*, 207−212.
(44) Miyauchi, M.; Nakajima, A.; Fujishima, A.; Hashimoto, K.; Watanabe, T. Photoinduced Surface Reactions on TiO_2 and $SrTiO_3$ Films: Photocatalytic Oxidation and Photoinduced Hydrophilicity. *Chem. Mater.* **2000**, *12*, 3−5.
(45) Miyauchi, M.; Nakajima, A.; Watanabe, T.; Hashimoto, K. Photocatalysis and Photoinduced Hydrophilicity of Various Metal Oxide Thin Films. *Chem. Mater.* **2002**, *14*, 2812−2816.

(46) Miyauchi, M.; Nakajima, A.; Watanabe, T.; Hashimoto, K. Photoinduced Hydrophilic Conversion of TiO_2/WO_3 Layered Thin Films. *Chem. Mater.* **2002**, *14*, 4714−4720.
(47) Mills, A.; Wang, J. Photobleaching of Methylene Blue Sensitized by TiO_2: an Ambiguous System. *J. Photochem. Photobiol., A* **1999**, *127*, 123−134.
(48) Mädler, L.; Kammler, H. K.; Mueller, R.; Pratsinis, S. E. Controlled Synthesis of Nanostructured Particles by Flame Spray Pyrolysis. *J. Aerosol Sci.* **2002**, *33*, 369−389.
(49) Wang, F.; Liu, B.; Zhao, C.; Yuan, S. Synthesis of $Zn_{1-x}Cd_xO$ bramble-like Nanostructures. *Mater. Lett.* **2009**, *63*, 1357−1359.
(50) Calareso, C.; Grasso, V.; Silipigni, L. The Cadmium Seleniophosphate ($CdPSe_3$) XPS and XAES Spectra. *Appl. Surf. Sci.* **2001**, *171*, 306−313.
(51) Singh, K. S. W.; Everett, D. H.; Haul, R. A. W.; Moscou, L.; Pierotti, R. A.; Rouquerol, J.; Sieminewska, T. Reporting Physisorption Data for Gas/Solid Systems with Special Reference to the Determination of Surface Area and Porosity. *Pure Appl. Chem.* **1985**, *57*, 603−619.
(52) Filho, N. L. D. Adsorption of Cu(II) and Co(II) Complexes on a Silica Gel Surface Chemically Modified with 2-mercaptoimidazole. *Microchim. Acta.* **1999**, *130*, 233−240.
(53) Sagripanti, J. L.; Routson, L. B.; Lytle, C. D. Virus Inactivation by Copper or Iron Ions Alone and in the Presence of Peroxide. *Appl. Environ. Microbiol.* **1993**, *59*, 4374−4376.
(54) Sawai, J. Quantitative Evaluation of Antibacterial Activities of Metallic Oxide Powders (ZnO, MgO and CaO) by Conductimetric Assay. *J. Microbiol. Methods* **2003**, *54*, 177−182.
(55) Makhluf, S.; Dror, R.; Nitzan, Y.; Abramovic, Y.; Jelinek, R.; Gedanken, A. Microwave-Assisted Synthesis of Nanocrystalline MgO and Its Use as Bacteriocide. *Adv. Funct. Mater.* **2005**, *15*, 1708−1715.
(56) Wong, M. S.; Chu, W. C.; Sun, D. S.; Huang, H. S.; Chen, J. H.; Tsai, P. J.; Lin, N. T.; Yu, M. S.; Hsu, S. F.; Wang, S. L.; Chang, H. H. Visible-Light-Induced Bactericidal Activity of a Nitrogen-Doped Titanium Photocatalyst Against Human Pathogens. *Appl. Environ. Microbiol.* **2006**, *72*, 6111−6116.
(57) Nel, A.; Xia, T.; Madler, L.; Li, N. Toxic Potential of Materials at the Nanolevel. *Science* **2006**, *311*, 622−627.